Supporting information to the manuscript "Nanoladder cantilevers made from diamond and silicon"

M. Héritier[1], A. Eichler[1], Y. Pan[2], U. Grob[1], I. Shorubalko[3], M. D. Krass[1], Y. Tao[2] and C. L. Degen[1]

[1]Department of Physics, ETH Zurich, Otto Stern-Weg 1, 8093 Zurich, Switzerland

[2]Rowland Institute at Harvard, 100 Edwin H. Land Blvd., Cambridge MA 02142, USA

[3]Swiss Federal Laboratories for Materials Science and Technology EMPA, Uberlandstrasse 129, 8600 Duebendorf, Switzerland

corresponding author adresses: eichlera@ethz.ch, tao@rowland.harvard.edu, degenc@ethz.ch

1. Device fabrication

1.1. Fabrication of single-crystal diamond nanoladders

Diamond devices were patterned by electron beam lithography onto an electronic-grade single crystal with a (100) surface orientation that was polished down to 20 μm thickness. The pattern was transferred to the diamond and released by inductively coupled plasma (ICP) etching. Detailed instructions can be found in Ref. [1, 2] with the important difference that the nanoladders were tethered to the support substrate (Fig. S1 (a)), in order to protect the fragile structure of the diamond nanoladders during the final release step. To cut the tether after the release, we used a focused helium ion beam (He-FIB) (Fig. S1 (b)). Zeiss Orion Plus He-FIB [3] equipped with a Raith Elphy MultiBeam pattern generator were used for presented study. He-FIB was operated at 30 kV acceleration voltage and $\sim 5 \times 10^{-5}$ Pa chamber pressure. He-ion beam current selected for this work was $5 - 10$ pA. It was defined by the following hardware parameters: 10 micrometer aperture, 6.7×10^{-4} Pa helium pressure in the gun chamber, and âĂIJspotâĂİ parameter between 2.5 and 3. The diamond cantilevers were cut by irradiating a box 500×100 nm with a dose $\sim 1\,\mathrm{C/cm^2}$. Such dose is expected to make a $200 - 400$ nm deep cut [4].

1.2. Fabrication of single-crystal silicon nanoladders

Silicon devices were batch-fabricated using single crystalline silicon-on-insulator (SOI) wafers (Soitec) with 1500 ± 30 nm device layer, 1000 ± 10 nm buried oxide layer, and 725 ± 15 μm handle layer. The device silicon layer was p-type, (100)-oriented, and had a resistivity of $18 \pm 4\,\mathrm{Ohm \cdot cm}$. A PECVD silicon nitride (SiNx) layer with 260 ± 10 nm thickness was deposited on the device layer of a 4-inch

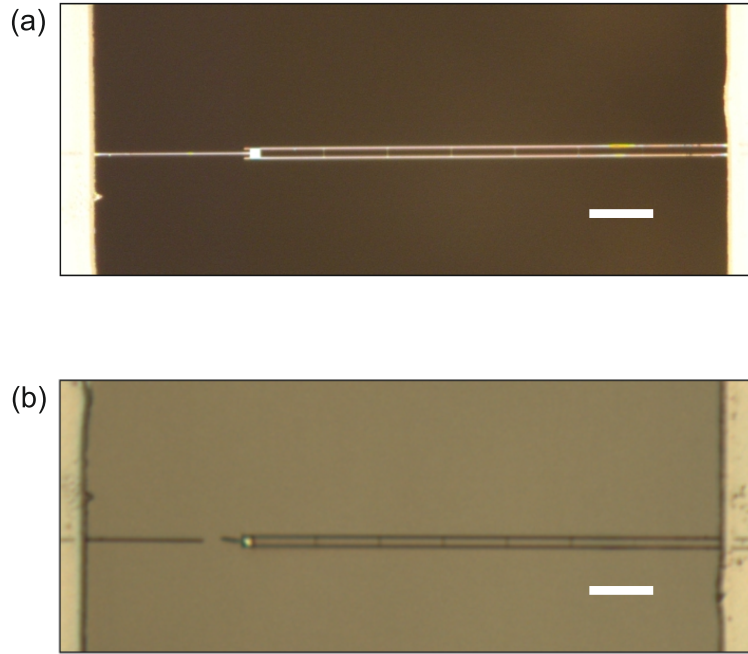

Figure S1: Focused ion beam cutting of diamond nanoladders. (a) Optical micrograph of a 150 μm diamond nanoladder cantilever after the final release. In order to protect the fragile structure, it was tethered to the opposite support substrate. (b) Optical micrograph of the same device after cutting by a focused helium ion beam which offers a high precision while inflicting minimal material damage. Scale bars are 20 μm.

SOI wafer and patterned by e-beam lithography (EBL). The device silicon layer was then wet-etched in tetramethyl ammonium hydroxide (TMAH) solution (25%, heated to 60 °C) with the patterned SiNx layer as a hard mask. The thickness of the device layer was monitored at different locations using profilometry in regular intervals during the silicon thinning process. This step determined the thickness of the nanoladders.

A layer of hydrogen silsesquioxane (HSQ), negative e-beam resist solution (6%) with 170 nm thickness was spin-coated (500 rpm, 5 s; 2000 rpm, 60 s) onto the SOI wafer with the thinned device layer. E-beam lithography was used to write the nanoladder features. After exposure, the sample was developed in a 351B:H2O solution (volume ratio 1 : 3) for 5 minutes. The resulting pattern served as a mask during the subsequent inductively coupled plasma (ICP) etching step, in which HBr plasma in the ICP was used to transfer the HSQ pattern into the underlying device layer. This is possible because HSQ is five times more etch-resistant than silicon. The residual HSQ mask was then removed by a short dipping (15 s) in buffered hydrofluoric acid (BHF). At this point, the silicon nanoladders remain anchored to the buried oxide layer (see Fig. S2 (a)).

The wafer was ready for backside etching to suspend the silicon nanoladders. To protect the patterned structures, AZ4562 resist was spin-coated at 4000 rpm onto the front side of the wafer. Thicker AZ4562 resist was spin-coated at 1500 rpm onto the backside to provide sufficient etch-resistance during DRIE. Following backside alignment and photolithography, the wafer was glued

Figure S2: Wafer-scale fabrication of silicon nanoladders. Optical micrograph of chips carrying 6 nanoladders of different lengths after electron beam lithography and inductively-coupled plasma etching step. The chip dimensions can be easily changed during fabrication to allow mounting them in a variety of systems. Scale bar: 2 mm

using wax to a dummy silicon carrier wafer via the front side. DRIE of the handle-layer silicon was performed to etch through the silicon down to the buried oxide stop layer.

To release the nanoladders, the wafer was soaked in warm NMP at 50 °C. The wafer was cleaned by rinsing, sequentially, in the following solvents: acetone, IPA, DI water, piranha solution, DI water, and IPA. The wafer was allowed to dry in air after taking it out from the final IPA rinse. To minimize contamination by drying residues, care was taken to keep the wafer tilted on a piece of cleanroom wipe to allow as much liquid to flow away as possible. Nitrogen flow was not used to avoid damaging the delicate buried oxide membranes. The wafer was etched in vapor HF for 10 minutes to remove the buried oxide layer, thus releasing the silicon nanoladders. Figures S3 (b) and (c) show optical micrographs of a wafer before and after this final step.

Taking advantage of the wafer-scale production, we designed some silicon nanoladders with a tether and some without (see Fig. S4). While the tethered devices could have been cut by a focused ion beam, a hydraulic micromanipulator system (Narishige Three-axis Hanging Joystick Oil Hydraulic Micromanipulator, model MMO-202ND) operated under an optical microscope yielded the same result.

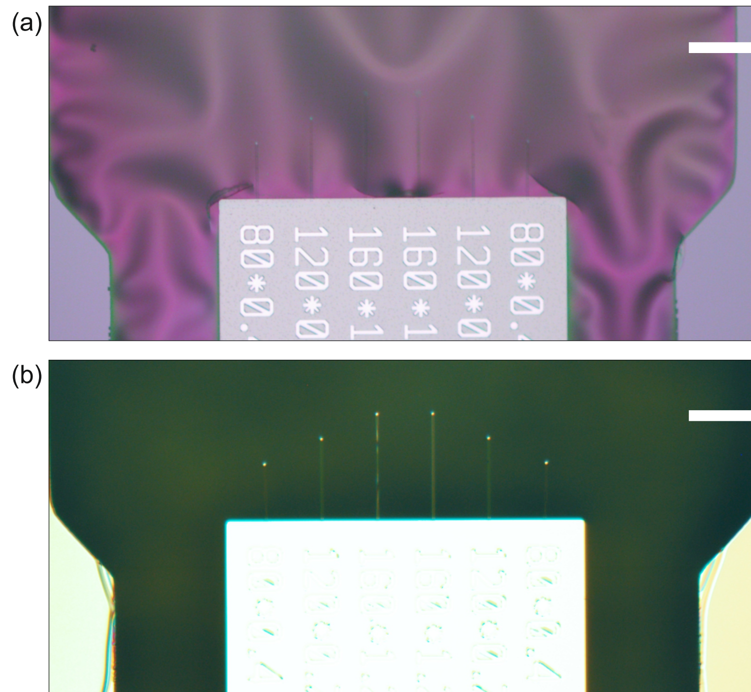

Figure S3: Final fabrication steps for silicon nanoladders. (a) Chip before the final vapor HF etch to remove the buried oxide layer and thus releasing the nanoladders. Scale bar: 100 μm (b) Ready-to-use chip after the final fabrication step. The chips can be easily picked out with a pair of tweezers and mounted into our custom-built AFM stage. Scale bar: 100 μm

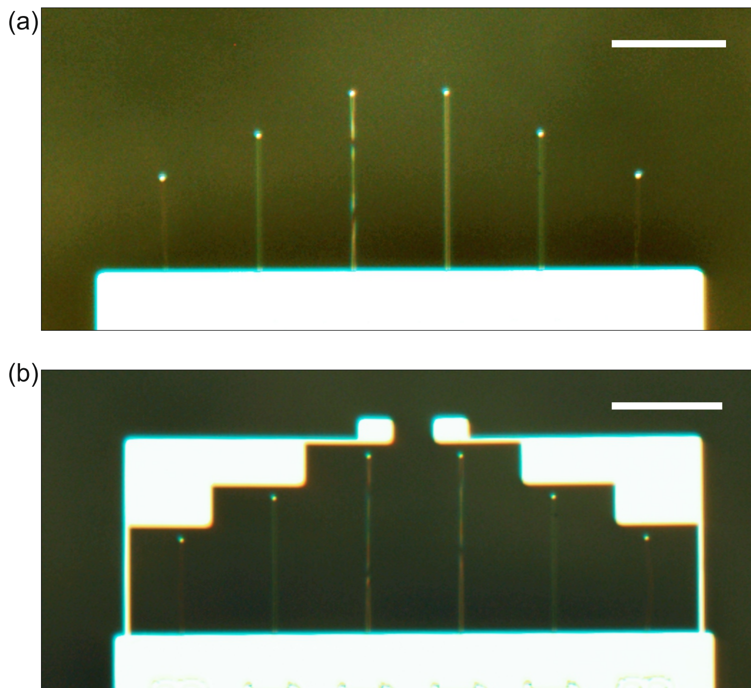

Figure S4: Tethering of devices. (a) Chip with finished silicon devices fabricated without tether. (b) Same devices but fabricated with help of a tether. Scale bars are 100 μm.

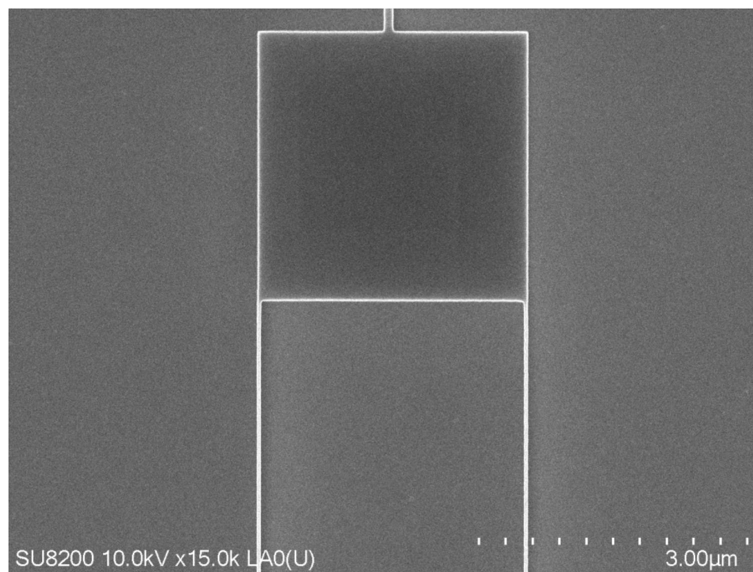

Figure S5: End mirror of the nanoladders. SEM micrograph of the paddle used for reflecting the readout laser beam from the cantilever. With a paddle area of 3×3 μm^2, the aspect ratio between the cantilever and the arms width is extreme. In this case, the arms width and thickness lie in the range of $50 - 60\,$nm, smaller than for the devices presented in the main manuscript which have a width and thickness in the range of $100 - 300\,$nm.

2. Characterization of further devices

We have investigated a total of 5 diamond and 2 silicon devices whose characteristics are shown in table S1. In particular, a 300 μm-long diamond cantilever has been characterized in the same manner as the devices of the main manuscript. It shows a similar behavior and agrees as well with our simulations. Its characteristics are summarized in table S2. The resonance frequency of the fundamental mode, $f_0 = 9,496.1\,\text{Hz}$, is measured from the thermomechanical displacement power spectral density shown in fig S6a.

Table S1: Characteristics of different devices at room temperature.

cantilever #	material	Length (μm)	f_c (kHz)	Q
1	diamond	100	25.22	$60,000$
2	diamond	150	13.914	$37,000$
3	diamond	250	4.640	$48,000$
4	diamond	300	4.180	$40,000$
5	diamond	300	9.500	$62,000$
6	silicon	160	4.282	$14,000$
7	silicon	160	5.523	$12,000$

Table S2: Key characteristics of a 300 μm long single crystal diamond nanoladder cantilever (cantilever #5 in table S1). ^{a} Reported Q factor represent the highest measured value at milikelvin temperatures.

					F_{th} (aN/$\sqrt{\text{Hz}}$)		
f_c (kHz)	m (pg)	k (μN/m)	Q^a	γ (pg/s)	300 K	4 K	100 mK
9.5	19.3	69	161,000	7.2	18	1.6	0.27

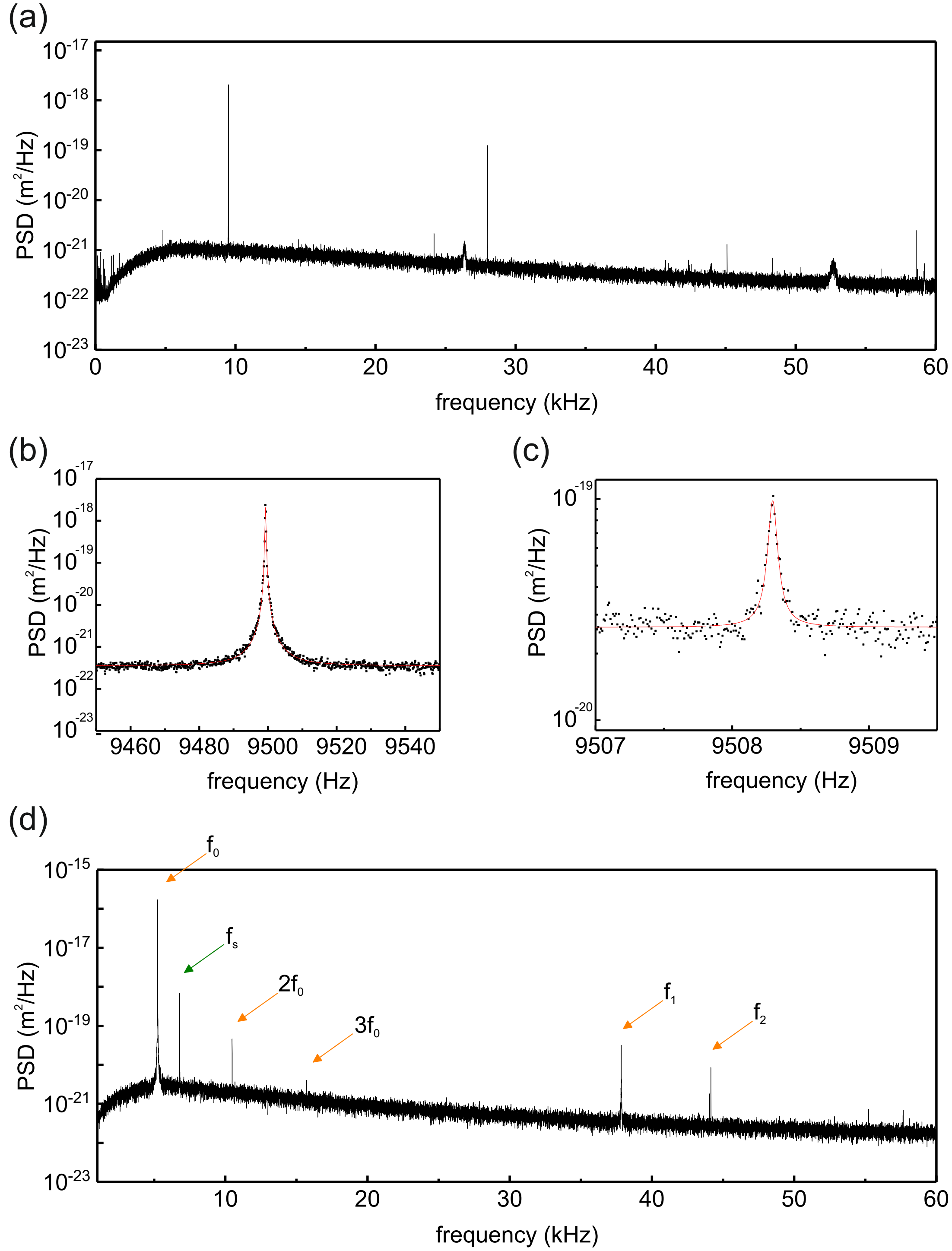

Figure S6: Characterization of a 300 μm-long diamond nanoladder cantilever (cantilever #5 in table S1). (a) Power spectral density (PSD) of the cantilever displacement measured at room temperature. (b) and (c) PSD of the fundamental mode ($f_0 = 9.499\,$kHz, $f_0 = 9.508\,$kHz) at room and cryogenic temperatures, respectively. (d) PSD of the silicon nanoladder cantilever at room temperature (device #6). Besides two harmonics of the fundamental resonance frequency ($2f_0$ and $3f_0$), the second ($f_1 = 37.83\,$kHz) and third ($f_2 = 44.23\,$kHz) modes are seen. The spurious mechanical resonance $f_s = 6.787\,$kHz with a quality factor of 7700 observed could correspond to one of the two other shorter devices present on the same chip.

3. Finite element modeling

3.1. Mode shape simulation

We performed finite element simulations to determine the mode shape of the nanoladders and their resonance frequencies. Figure S7 shows the results where (a) corresponds to the fundamental resonance frequency, and (b)-(f) show increasingly higher modes. (a), (c), and (f) correspond to in-plane motion whereas (b), (d), and (e) include only lateral motion. The fundamental mode has approximately the same shape as the one of a plain beam cantilever.

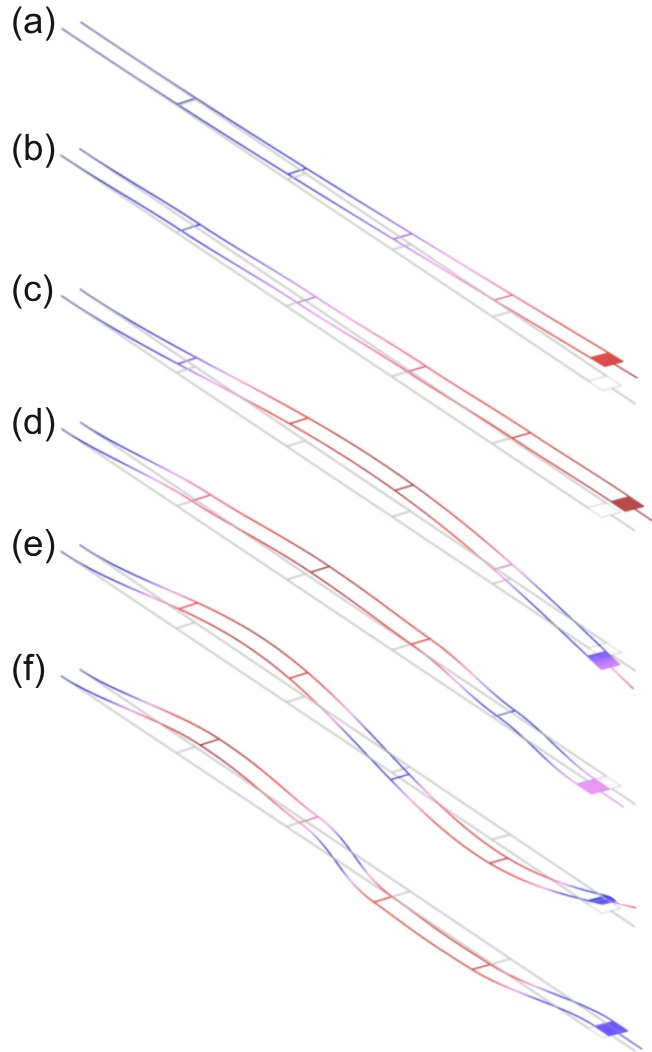

Figure S7: COMSOL mode shape simulation of the fundamental and higher modes. (a) Fundamental mode, $f_c^{(a)} = 25.4\,\mathrm{kHz}$, (b) $f_c^{(b)} = 142\,\mathrm{kHz}$, (c) $f_c^{(c)} = 204\,\mathrm{kHz}$, (d) $f_c^{(d)} = 488\,\mathrm{kHz}$, (e) $f_c^{(e)} = 619\,\mathrm{kHz}$, (f) $f_c^{(f)} = 905\,\mathrm{kHz}$. (a), (c), and (f) correspond to in-plane motion whereas (b), (d), and (e) include only lateral motion.

3.2. Estimations of resonance frequency and spring constant

We compare our results to theoretical simulations by two different approaches. In a first approximation, the rungs and the paddle are neglected and the nanoladder is considered as two single beams coupled in parallel. The effective spring constant k writes then $k = 2k_{\text{beam}}$ where k_{beam} is the spring constant of a single beam. It is given by

$$k_{\text{beam}} = W \left(\frac{T}{L}\right)^3 \frac{E}{4} \tag{1}$$

with W being the width, T the thickness, L the length and E the Young's modulus of the beam. The fundamental mode frequency reads

$$f_0 = 0.162 \frac{T}{L^2} \sqrt{\frac{E}{\rho}} \tag{2}$$

where ρ is the Poisson's ratio of the material. Fixing the length to 100 μm or 300 μm, respectively, we computed lower and upper boundaries for frequency and spring constant by setting the width and the thickness to 100 nm and 300 nm, respectively.

The second method is a finite element simulation performed for the same parameters through COMSOL. The simulated results are shown in table S3 and are compared to the measured values.

Table S3: Simulated cantilever characteristics compared to the measured values. [a]Device # in table S1)

Device[a]	f_c (kHz)			k (μN/m)		
	analytical	COMSOL	measured	analytical	COMSOL	measured
#1	30.1-90.4	16.9-68.0	25.2	61-4940	85-8918	106
#5	3.35-10	2.45-22.6	9.50	2.26-183	3.90-404	69
#7	5.06-15.2	3.30-12.5	5.46	10.2-710	2.88-297	6.5

4. Quality factor study

We have studied the quality factor dependance on temperature for our different devices as shown in fig S8 (a). It increases from room temperature towards cryogenic temperatures for all 3 devices. The dip around 150 K has been previously observed in single-crystal diamond (electronic and optical grade), polycrystalline diamond and single-crystal silicon. The feature has been ascribed to dissipation caused by surface adsorbates or a surface passivation layer [2, 5]. Around 230 K, an interferometer malfunction prevented a precise measurement and we therefore removed the data in the relevant temperature range.

As shown in the main manuscript, the mode temperature of the cantilever depends on the incident laser power in the milikelvin range. During this measurement, we have monitored the quality factor as well as seen in fig S8 (b). The quality factor increases for decreasing mode temperatures. No change of the quality factor is observed at room temperature and at 4 K. This corresponds to the expectation that the absorption of the laser light is negligible at those temperatures.

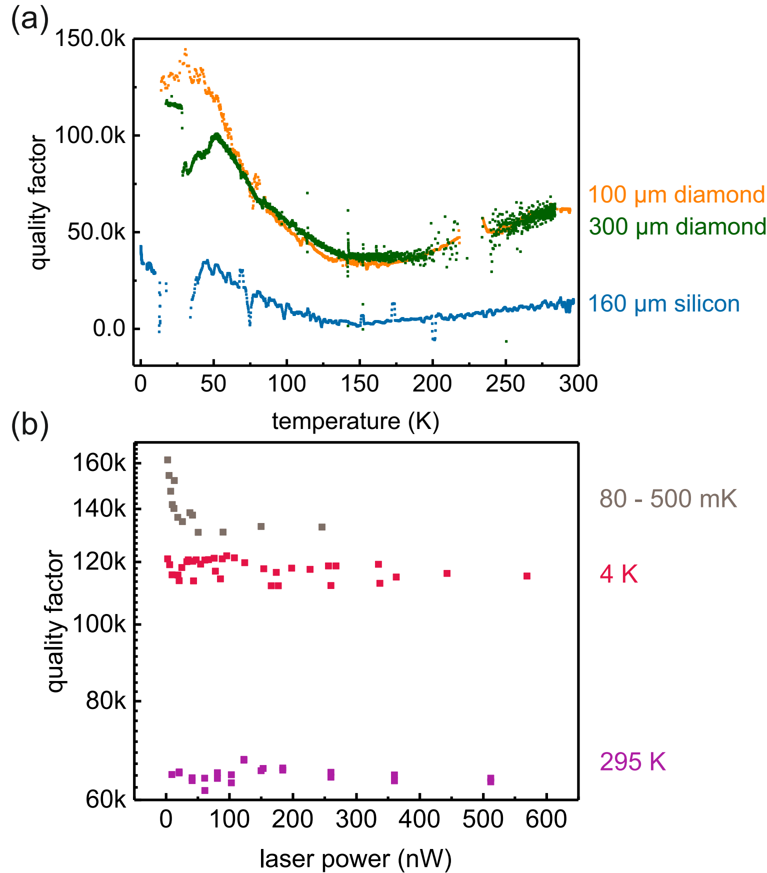

Figure S8: Quality factor measurements. (a) Q between 4 and 300 K. Orange corresponds to device #1, green to #5 and blue to #6. (b) Q as function of the laser power at different temperature ranges. The purple squares correspond to values at room temperature, the red ones were taken at 4 K, and the light gray denote milikelvin temperature measurements. While no change is observed for 300 and 4 K, Q increases with decreasing laser power in the milikelvin range.

5. Estimation of mode temperature and force noise

This Section discusses how the values and errors reported for cantilever mass, spring constant, mode temperature and force noise were calculated.

5.1. Room temperature calibration

In a first step, the mass m and spring constant k of the resonator were determined by a room temperature measurement of the displacement power spectral density (PSD). The room-temperature spring constant k_{RT} and mass m are given by

$$k_{\mathrm{RT}} = \frac{k_{\mathrm{B}} T_{\mathrm{RT}}}{(V_{\mathrm{rms,RT}} s_{\mathrm{RT}} c_{\mathrm{RT}})^2} \tag{3}$$

$$m = \frac{k_{\mathrm{RT}}}{(2\pi f_{c,\mathrm{RT}})^2} \tag{4}$$

where k_{B} is Boltzmann's constant, $T_{\mathrm{RT}} = 295\,\mathrm{K}$, $f_{c,\mathrm{RT}}$ is the resonance frequency, $V_{\mathrm{rms,RT}}$ the rms value of the displacement measured in units of Volts, s_{RT} the interferometer displacement sensitivity in units of meters per Volt, and c_{RT} the c-factor, a geometrical factor accounting for the mode shape at the location of the laser spot used for readout. The rms displacement $V_{\mathrm{rms,RT}}$ was calculated by integrating the displacement PSD. $V_{\mathrm{rms,RT}}$ corresponds to the area under the peak after the baseline has been substracted (see Fig. S10). To determine $V_{\mathrm{rms,RT}}$, the voltage PSD $\mathrm{S_V}(f)$ was numerically integrated around the resonance with a bandwidth B to get the power P_1,

$$P_1 = \sum_{f_c - B/2}^{f_c + B/2} \mathrm{S_V}(f) \Delta f \tag{5}$$

where the sum runs over N points in the interval $[f_{\mathrm{c}} - B/2, f_{\mathrm{c}} + B/2]$ and $\Delta f = B/N$ is the frequency sampling of the PSD. To determine the baseline, two additional noise powers were calculated,

$$P_2 = \sum_{f_c - 3B/2}^{f_c - B/2} \mathrm{S_V}(f) \Delta f \tag{6}$$

$$P_3 = \sum_{f_c + B/2}^{f_c + 3B/2} \mathrm{S_V}(f) \Delta f \tag{7}$$

corresponding to the areas to the left and right of the signal peak, respectively (see Fig. S10). The rms value of the displacement is then

$$V_{\rm rms} = \sqrt{P_1 - (P_2 + P_3)/2}. \tag{8}$$

The displacement sensitivity $s_{\rm RT}$ was determined by sweeping the wavelength of the interferometer, which we achieved by controlling the temperature of the laser diode via a thermoelectric cooler (TEC). Due to additional stray reflections in our experimental setup, we observed variations in the slopes of the individual fringes $a_{\rm i} = 2\pi V_{\rm pp,i}/\lambda$, where $V_{\rm pp,i}$ is the peak-to-peak voltage of the i-th fringe and $\lambda = 1550\,{\rm nm}$ is the laser wavelength (whose variance between fringes is negligible). These artifacts should not be present when changing the interferometer length instead of the wavelength. To cancel them out, we calculated the mean value of all slopes within 4-5 fringes, $a = \frac{1}{N}\sum_{i=1}^{N} a_{\rm i}$, and used the result to determine the displacement sensitivity $s_{\rm RT} = G/a$, where G is a factor accounting for the different gains used for the calibration (DC signal) and the cantilever displacement measurements (AC signal), typically $G = 0.1$. The value of a was in agreement with a separate calibration method, which consisted in driving the cantilever until its vibration amplitude exceeded the fringe. Since we observed that the sensitivity determined from the slope would vary with a standard deviation of 15% between measurements, we use $\sigma_{s_{\rm RT}} = 0.15 s_{\rm RT}$. Note that the same uncertainty applies to $s_{\rm mK}$.

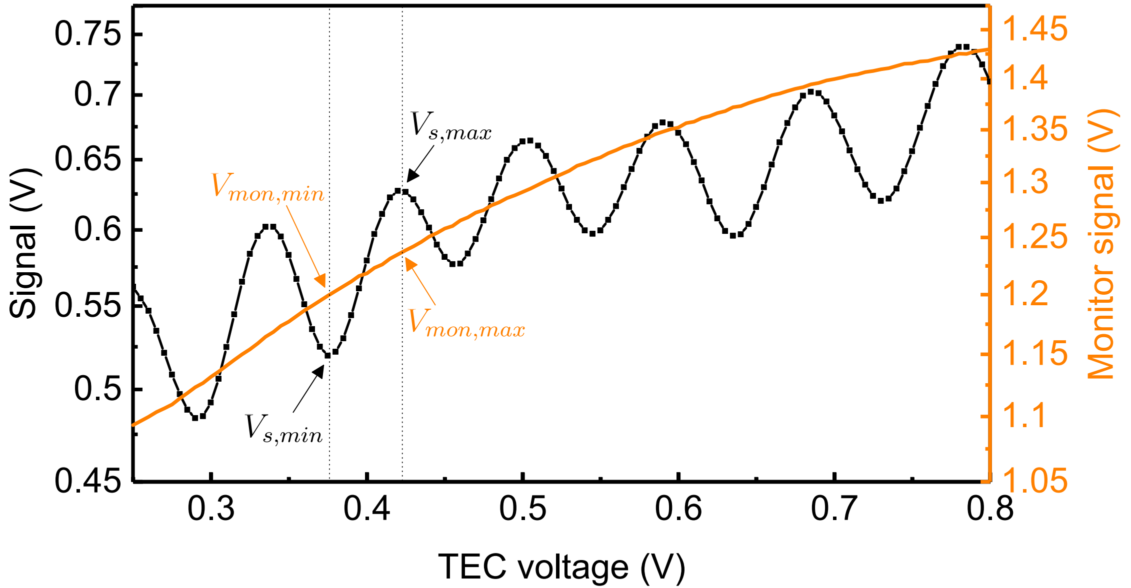

Figure S9: Calibration of the displacement sensitivity. A fringe pattern is measured when sweeping the laser wavelength, which is achieved by adjusting the temperature of the laser diode with a thermoelectric cooler (TEC). The mean displacement sensitivity is then determined from the slopes of several individual fringes (see text). The measured signal is shown in black and the laser power monitor signal in orange.

As shown in fig. S9, the fringe signal features a general upwards slope with increasing TEC voltage.

This slope is due to a dependence of the laser power on the TEC voltage. To correct for this effect, we monitored the laser output power (before the interferometer) with a separate detector and used this monitor signal (orange curve in fig. S9) to normalize the fringe voltage. For every individual fringe, we computed the peak-to-peak voltages as

$$V_{\mathrm{pp}} = \left(\frac{V_{\mathrm{s,max}}}{V_{\mathrm{mon,max}}} - \frac{V_{\mathrm{s,min}}}{V_{\mathrm{mon,min}}} \right) V_{\mathrm{mon,avg}} \tag{9}$$

where $V_{\mathrm{mon,avg}}$ is the monitor voltage in the center of the fringe. For convenience, we have dropped the index i in this equation.

The c-factor was computed based on the location of the reflective paddle and was $c = 1.07$ for diamond and $c = 1.04$ for silicon at room temperature.

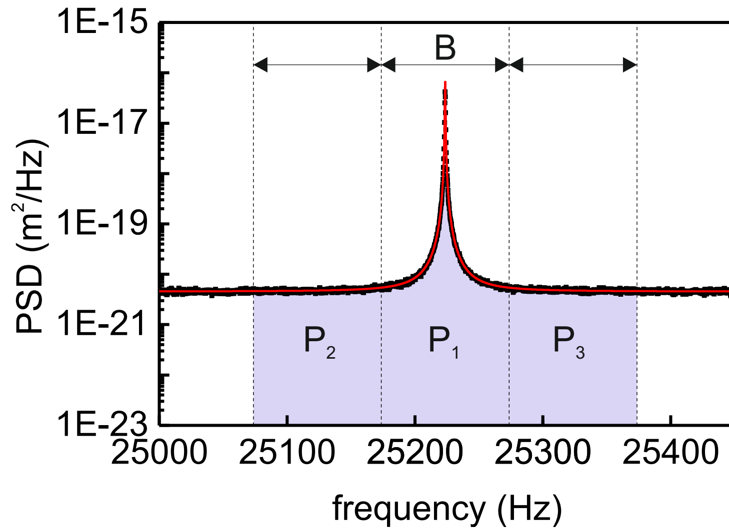

Figure S10: Integration of the power spectral density. All 3 powers $P_{1,2,3}$ are computed by integrating the power spectral density over the same interval B. The power under the peak is P_1 and $P_{2,3}$ are the baseline powers. Data are for device #1.

5.2. Errors of spring constant and mass

The dominant contribution to the errors in the estimates for spring constant and mass is the uncertainty in the displacement sensitivity s_{RT}. Because of the low reflection of the mirror paddle and due to additional stray reflections in our experimental setup, the displacement sensitivity could vary with a standard deviation of about 15% between different measurements (see previous section for details). We therefore assume an error $\sigma_{s_{\mathrm{RT}}} = 0.15 s_{\mathrm{RT}}$ for the following error calculation. The errors in the c-factor c_{RT} and the rms displacement V_{rms} were comparably much smaller, typically $\sigma_{c_{\mathrm{RT}}} < 0.01 c_{\mathrm{RT}}$ and $\sigma_{V_{\mathrm{rms,RT}}} < 5 \cdot 10^{-4} V_{\mathrm{rms,RT}}$, and are neglected in the following. The propagated

error is

$$\sigma_{k_{\mathrm{RT}}} \approx \frac{2k_{\mathrm{B}}T_{\mathrm{RT}}}{s_{\mathrm{RT}}^{3}(V_{\mathrm{rms,RT}}c_{\mathrm{RT}})^{2}}\sigma_{s_{\mathrm{RT}}} \tag{10}$$

The corresponding error for the mass is

$$\sigma_{m} = \frac{\sigma_{k_{\mathrm{RT}}}}{(2\pi f_{c,\mathrm{RT}})^{2}} \tag{11}$$

5.3. Low-temperature measurement

To determine the mode temperature and thermal force noise at millikelvin temperatures, we used the room-temperature calibration of k_{RT} and m together with a low-temperature measurement of the displacement PSD. The mode temperature T_{mK} and thermal force noise PSD $S_{F,\mathrm{mK}}$ are given by

$$T_{\mathrm{mK}} = \frac{k_{\mathrm{mK}}(V_{\mathrm{rms,mK}}s_{\mathrm{mK}}c_{\mathrm{mK}})^{2}}{k_{\mathrm{B}}} \tag{12}$$

$$S_{F,\mathrm{mK}} = \left[\frac{4k_{\mathrm{mK}}^{2}(V_{\mathrm{rms,mK}}s_{\mathrm{mK}}c_{\mathrm{mK}})^{2}}{(2\pi f_{c,\mathrm{mK}})Q_{\mathrm{mK}}}\right]^{1/2} \tag{13}$$

where $k_{\mathrm{mK}} = k_{\mathrm{RT}}(f_{c,\mathrm{mK}}/f_{c,\mathrm{RT}})^{2}$ is the low-temperature spring constant, and $V_{\mathrm{rms,mK}}$, s_{mK} and c_{mK} are the corresponding displacement noise, displacement sensitivity and c-factor for the low-temperature measurement. Q_{mK} is the low-temperature quality factor that was determined in a separate ring-down measurement.

The principal uncertainties in T_{mK} and $S_{F,\mathrm{mK}}$ are the calibration uncertainty in k_{RT} and the uncertainty in the displacement sensitivity s_{mK}. Error propagation yields

$$\sigma_{T_{\mathrm{mK}}} = \frac{1}{k_{\mathrm{B}}}\left[(V_{\mathrm{rms,mK}}s_{\mathrm{mK}}c_{\mathrm{mK}})^{4}\sigma_{k_{\mathrm{mK}}}^{2} + (2k_{\mathrm{mK}}s_{\mathrm{mK}}V_{\mathrm{rms,mK}}^{2}c_{\mathrm{mK}}^{2})^{2}\sigma_{s_{\mathrm{mK}}}^{2}\right]^{1/2} \tag{14}$$

$$\sigma_{S_{F,\mathrm{mK}}} = \left[\left(\frac{2(V_{\mathrm{rms,mK}}c_{\mathrm{mK}}s_{\mathrm{mK}})^{2}}{\pi f_{c,\mathrm{mK}}Q_{\mathrm{mK}}}\right)\sigma_{k_{mK}}^{2} + \left(\frac{2(k_{\mathrm{mK}}V_{\mathrm{rms,mK}}c_{\mathrm{mK}})^{2}}{\pi f_{c,\mathrm{mK}}Q_{\mathrm{mK}}}\right)\sigma_{s_{\mathrm{mK}}}^{2}\right]^{1/2} \tag{15}$$

5.4. Monte Carlo-based error propagation

Because of the significant uncertainty in the calibration of the displacement sensitivities s_{RT} and s_{mK}, we performed a Monte Carlo simulation of the uncertainty in the force noise in addition to a standard error propagation calculation. We found that the Monte Carlo method gives slightly different, but similar values to the standard error propagation. Errors reported in the manuscript represent the values of the Monte Carlo simulation.

5.5. Thermal force noise vs. force sensitivity

The total noise power spectral density (PSD) measured at the output of the interferometer is the sum of the transduced displacement noise PSD of the cantilever $S_{v,th}$ (caused by the thermal force noise) and the detector noise PSD intrinsic to the interferometer $S_{v,det}$,

$$S_{v,tot} = S_{v,th}G^2 + S_{v,det}. \tag{16}$$

Here, we use $G = s_{\mathrm{mK}}^{-1}$ ($G = s_{\mathrm{RT}}^{-1}$ at room temperature) for the total transducer gain of the interferometer in units of V/m and the units of $S_{v,th}$ and $S_{v,det}$ are m^2/Hz and V^2/Hz, respectively. In order to be detectable, a force signal must cause a displacement signal that is larger than the standard deviation of the total noise measured with a certain bandwidth B, which according to Parseval's theorem is given by

$$\int_B S_{v,tot}(f)df. \tag{17}$$

In the narrow-filter limit ($B \ll f_0/Q$) and defining the force sensitivity as the smallest measurable force which can be detected with unit signal-to-noise ratio per bandwidth, $F_{\min}$, we get

$$F_{\min} = \left[B(S_{F,th} + \frac{k^2}{Q^2}\frac{S_{v,det}}{G^2})\right]^{1/2} \tag{18}$$

where $S_{F,th} = 4k_BT\gamma$ is the white thermal force noise PSD and $S_{v,det}$ is the displacement noise PSD of the interferometer determined by the baseline in Fig. S10 (note that $S_{v,det}$ does not correspond to a real cantilever displacement but to a displacement uncertainty caused by the detector noise). Since $S_{F,th}$ generates a peak of magnitude $S_{v,th,peak} = G^2(Q/k)^2S_{F,th}$ in the real displacement PSD, the force sensitivity can be expressed as

$$F_{\min} = F_{\mathrm{th}}\left[1 + \frac{S_{v,det}}{S_{v,th,peak}}\right]^{1/2} \tag{19}$$

where we have used the notation $F_{\mathrm{th}} = \sqrt{S_{F,th}B}$ for the force noise. Thus, in the absence of significant detector noise ($S_{v,det} \ll S_{v,th,peak}$), force noise and force sensitivity are equal, $F_{\min} \approx F_{\mathrm{th}}$. In the presence of detector noise, the force sensitivity is worse than the thermal force noise by a factor of $[1 + \frac{S_{v,det}}{S_{v,th,peak}}]^{1/2}$.

References

[1] Tao, Y.; Degen, C. Advanced Mater. **2013**, 25, 3962-3967.

[2] Tao, Y.; Boss, J.; Moores, B.; Degen, C. Nature Commun. **2014**, 5, 3638.

[3] Hill, R.; Notte, J.; Ward, B. Phys Procedia. **2008**, 1, 135-141.

[4] Scholder, O.; Jefimovs, K.; Shorubalko, I.; Hafner, C.; Sennhauser, U.; Bona, G. L. Nanotechnology **2013**, 24, 395301.

[5] Tao, Y.; Navaretti, P.; Hauert, R.; Grob, U.; Poggio, M.; Degen, C. L. Nanotechnology **2015**, 26, 46550.